Supplementary Information

Ultrahigh-efficiency desalination via a thermally-localized multistage solar still

Zhenyuan Xu[†,1,2], Lenan Zhang[†,2], Lin Zhao[†,2], Bangjun Li[†,1], Bikram Bhatia[2], Chenxi Wang[1], Kyle L. Wilke[2], Youngsup Song[2], Omar Labban[2], John H. Lienhard[2], Ruzhu Wang[*,1], Evelyn N. Wang[*,2]

[1]Institute of Refrigeration and Cryogenics, Shanghai Jiao Tong University, Shanghai 200240, China

[2]Department of Mechanical Engineering, Massachusetts Institute of Technology, Cambridge, MA 02139, USA

[†]These authors contributed equally to this work

[*]e-mail: rzwang@sjtu.edu.cn (R. Wang); enwang@mit.edu (E.N. Wang)

Supplementary Note S.1

Heat and Mass Transport Model and System-level Optimization

To understand the fundamental heat and mass transport and optimize the thermally-localized multistage solar still (TMSS), we developed a theoretical model in our prior work [1]. In this section, we provide a brief description of the overall modelling framework and discuss several key results. As shown in Fig. S1, the model considers an *n*-stage TMSS device with solar absorbing area $a \times a$, and air gap thickness b. To simplify the problem, we assumed the condenser has the same temperature as its adjacent evaporator since the evaporator and the condenser are very thin (≈ 0.1 mm) and in thermal contact. T_i represents the evaporator temperature of i^{th} stage ($i = 1 \sim n$) and T_b indicates the temperature of the last condenser. We considered various heat losses including convection (q''_{conv}) and radiation (q''_{rad}) from the front solar absorber as well as heat loss ($q''_{side,i}$) from the sidewall of each stage. Heat conduction through the air gap ($q''_{cond,i}$) was also modelled. The energy balance of each stage can be expressed as,

$$\begin{cases} a^2 q_i'' = a^2\left(q''_{rad} + q''_{conv} + q''_{cond,i} + q''_{evap,i}\right) + 4abq''_{side,i}, & (i = 1) \\ a^2 q_i'' = a^2\left(q''_{cond,i} + q''_{evap,i}\right) + 4abq''_{side,i}, & (i > 1) \\ q''_{i+1} = q''_{cond,i} + q''_{evap,i}, \end{cases} \quad \text{(S1)}$$

where $q''_{evap,i}$ is the heat flux carried by vaporization at i^{th} stage which can be expressed as,

$$q''_{evap,i} = h_{fg} m''_{evap,i} \quad \text{(S2)}$$

where m''_{evap} is the evaporative mass flux, and h_{fg} is the vaporization enthalpy. m''_{evap} can be calculated using Fick's law of diffusion,

$$m''_{evap,i} = -D_a \frac{dc}{dx} \approx D_a \frac{c_e - c_c}{b} \quad \text{(S3)}$$

where D_a is the mass diffusivity. c_e and c_c are the saturated vapor concentration on the evaporator and the condenser, respectively, which are determined by the evaporator and condenser temperatures. The radiation heat loss from the solar absorber is given by,

$$q''_{rad} = \varepsilon\sigma(T_1^4 - T_\infty^4) \quad \text{(S4)}$$

where ε is the emissivity, $\sigma = 5.67 \times 10^{-8}\, Wm^{-2}K^{-4}$ is the Stefan-Boltzmann constant, and T_∞ is the ambient temperature. Heat convection on the solar absorber can be expressed as,

$$q''_{conv} = h_a(T_1 - T_\infty) \tag{S5}$$

where h_a is the convective heat transfer coefficient of air, which can be obtained from the correlation $Nu = 0.59Ra^{\frac{1}{4}}$ (Nu is the Nusselt number and Ra is the Rayleigh number) [2]. The heat loss through the sidewall can be estimated as,

$$q''_{side,i} = \frac{\bar{T}_i - T_\infty}{R_{side}} \tag{S6}$$

where $\bar{T}_i$ is the average side wall temperature $\frac{T_i + T_{i+1}}{2}$, and R_{side} is the total thermal resistance per unit area of the side wall insulation and the ambient air,

$$R_{side} = \frac{1}{h_a} + \frac{t}{k} \tag{S7}$$

where *t* is the thickness and *k* is the thermal conductivity of the sidewall. The heat conduction through the air gap is given by Fourier's law,

$$q''_{cond,i} = -k_a \frac{dT}{dx} \approx k_a \frac{T_i - T_{i+1}}{b} \tag{S8}$$

where k_a is the thermal conductivity of air. The input of this model are material properties including D_a, h_a, k_a, k and ε, geometrical configuration including a, b, and t, and the ambient temperature T_∞. The input heat flux $q''_1 = \alpha q''_{sun}$ is given by the absorption coefficient of the solar absorber α, and the incident solar flux q''_{sun}. Since the last condenser is inserted into the water reservoir, we assumed $T_b \approx T_\infty$ in our calculation. Substituting Eqs. (S2)-(S8) into Eq. (S1), we obtained the governing equations that describe the heat and mass transfer through each stage, that were solved iteratively to predict the performance of TMSS.

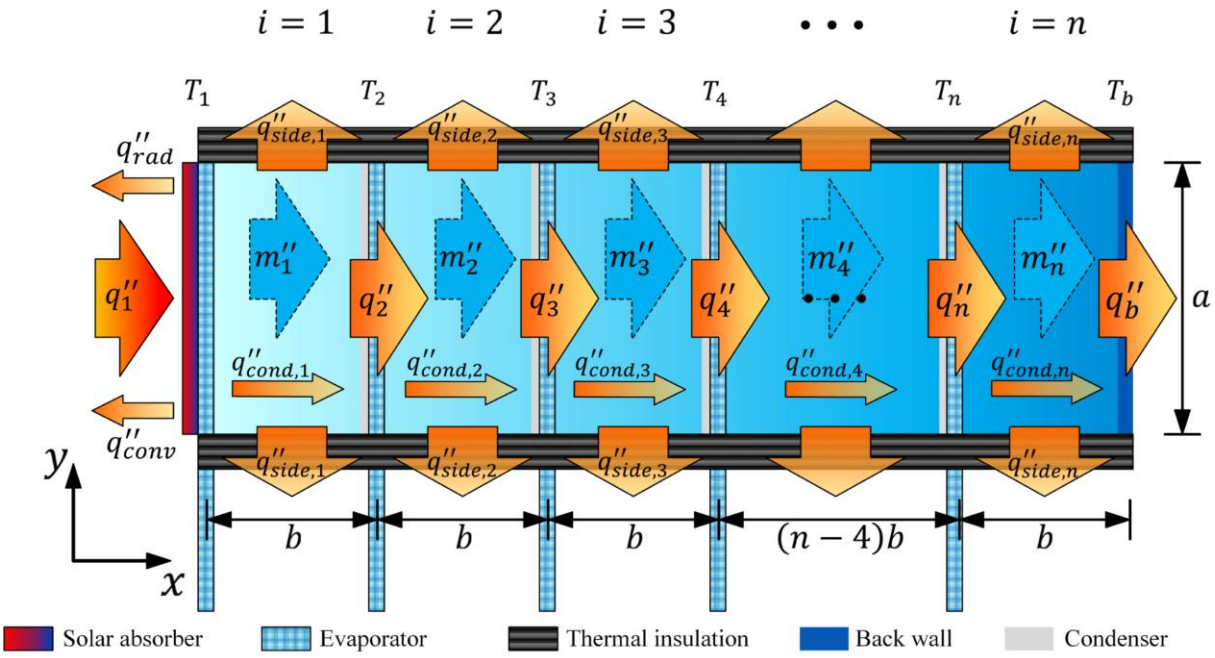

Fig. S1 Schematic of the heat and mass transfer in the TMSS device. The modelling framework considers various heat loss mechanisms including radiation and convection from the solar absorber, heat loss from the sidewall and heat conduction through the air gap. The model based on energy conservation uses the material properties and geometrical configuration as the input. The temperature and heat flux of each stage were solved iteratively.

The model described above provided insights into the heat and mass transfer within the TMSS device and enabled performance optimization. Fig. S2 shows representative modeling results for the nominal device configuration and using the parameters listed in Table S1. Model results (Fig. S2(a)) show that, for a fixed geometrical configuration (a = 10 cm and b = 2.5 mm in this example), the solar thermal efficiency increases as the number of stages increase and plateaus at a peak efficiency (650% in this example). The benefit of adding more stages diminishes beyond a certain number of stages since the vaporization enthalpy recovered by each subsequent stage is negligible in comparison to the heat loss through the sidewalls. In comparison with a single-stage device, the solar thermal efficiency of a ten-stage configuration is > 5× higher – about 450%, in comparison to 80% for a single-stage device. However, with further increase in n to 20, the additional efficiency enhancement is only 180% even though the total number of stages is doubled. When n > 20, the relative performance improvement is insignificant.

Table S1. Simulation parameters for TMSS device optimization

Parameter	Value	Parameter	Value
$q''_{sun}\ (W/m^2)$	1000	$h_a\ (W/m^2K)$	5.37
T_b (°C)	23	$k_a\ (W/mK)$	0.026
T_∞ (°C)	23	$t\ (cm)$	1.27
$a\ (cm)$	10	$k\ (W/mK)$	0.022
$b\ (mm)$	2.5	ε	0.03
$D_a\ (m^2/s)$	3.0×10^{-5}	α	0.97
$h_{fg}\ (kJ/kg)$	2394	n	10

Since the peak efficiency is determined by the geometrical configuration, we studied the peak efficiency as a function of air gap thickness *b* (Fig. S2(b)). At first, the peak efficiency increases with *b* (when $b < 2.5$ mm) due to the decrease in conduction loss through the gap, but subsequently decreases (when $b > 2.5$ mm) due to the increase of vapor transport resistance – leading to a global optimum at $b = 2.5$ mm. A similar optimum *b* (about 2.5 mm) is observed for a ten-stage device that maximizes its solar thermal efficiency ($\eta \approx 450\%$). For the device configuration used in our experiments ($n = 10$ and $b = 5$ mm), the predicted solar thermal efficiency is about 417%.

The overall device performance is a strong function of sidewall thermal insulation. Fig. S2(c) shows the effect of sidewall thermal insulation (thermal conductivity, $k = 0.022$ W m^{-1} K^{-1}) on the solar thermal efficiency as the insulation thickness *t* is varied from 0 to 10 cm. For the 1.27 cm thick thermal insulation we used in our experiments (indicated by the star on the plot), a 100% improvement in solar thermal efficiency can be achieved over the uninsulated case (Figs. 3(e) and S2(c)). The overall performance enhancement becomes insignificant when the sidewall insulation thickness is larger than 1.5 cm.

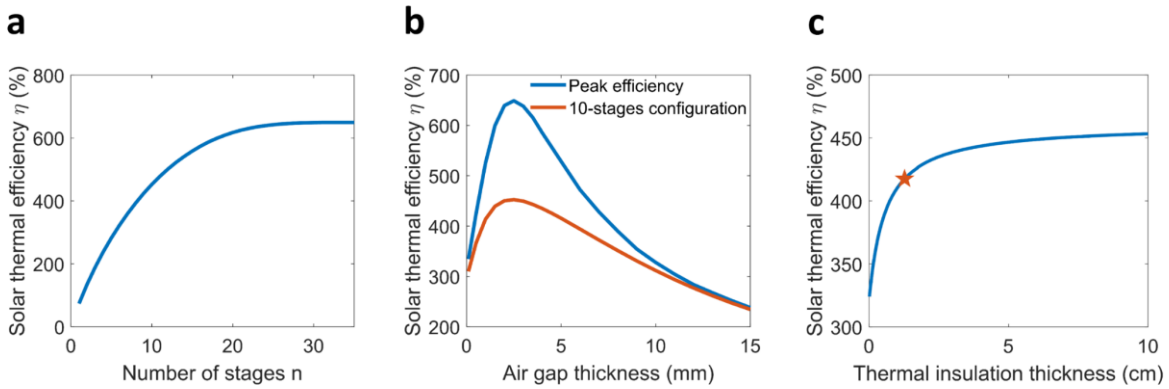

Fig. S2 Theoretical optimization of the TMSS device. (a) Increase in solar thermal efficiency with the number of stages for a TMSS device with width a = 10 cm and air gap thickness b = 2.5 mm. Performance enhancement becomes insignificant when n > 20 due to the heat loss from the sidewalls. (b) Effect of the air gap thickness b on the peak solar thermal efficiency of the TMSS device. The global optimized gap thickness is about 2.5 mm. (c) Effect of sidewall thermal insulation on the overall performance. The red star indicates the predicted solar thermal efficiency (417%) with 1.27 cm thick thermal insulation (k = 0.022 W m^{-1} K^{-1}).

Supplementary Note S.2

Design and Fabrication of the TMSS Prototype

Fig. S3 shows the detailed design for the TMSS prototype frames that were 3D-printed using Nylon 12 (Shenzhen Wenext Technology Co., Ltd.). The frames were designed to have a discontinuous hollow structure (represented by the red-dashed region) for better thermal insulation and reduce material cost. Since the first stage includes the solar absorber and the last stage includes the condenser that dissipates heat to the water reservoir, the design of the first and last stages is different from that of the middle stages. Front and side views of the first-stage frame (Fig. S3 (a)) show the seven screw holes at the top, left and right sides to connect different stages together. A slot on the front side is used to hold the glass cover and a slot on the backside is used to hold the solar absorber (10×10 cm^2) – leaving an aperture area of 9.6×9.6 cm^2 for solar absorption. Front and side views of the middle-stage frame (Fig. S3 (b)) showing a 0.3 cm wide groove, with a 5.7^o tilt angle, at the bottom which is used to transport and collect water from the bottom of the condenser. An outlet (0.2×0.3 cm^2) at the end of the groove was used to let the water flow out (Fig. S3(b)). A triangular guard was additionally added at the corner near the outlet (Fig. S3(b) and S3(c)) to prevent water accumulation or leaking close to the outlet due to capillary pressure. Front and side views of the last-stage frame (Fig. S3 (c)) showing a structure similar to the middle-stage including seven screw holes on the sides to clamp all of the stages together.

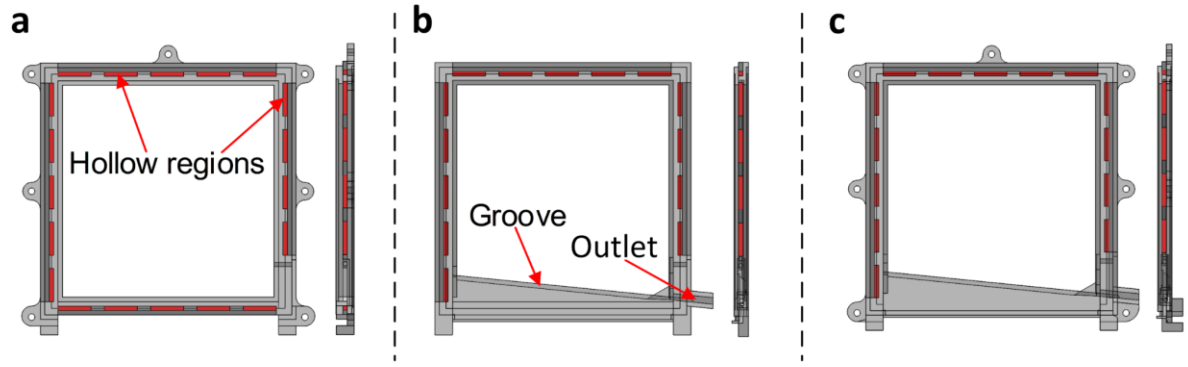

Fig. S3 Detailed design of the TMSS prototype frame. Front and side views of the (a) first-stage frame, (b) middle-stage frame, and (c) last-stage frame.

Fig. S4 shows the 10-stage TMSS prototype assembly. The key components of the first stage (Fig. S4(a)) include a solar absorber (B-SX/T-L/Z-Z-1.88, Linuo-Paradigma, $10\times10\times0.05$ cm^3),

embedded at the back of the frame, that was attached with a paper towel (10×15×0.05 cm^3) which served as the evaporator. A monolithic silica aerogel (10×10×0.5 cm^3) covered the front of the solar absorber that minimized thermal losses. Anti-reflection (AR) glass cover (10×10×0.1 cm^3) enclosed the aerogel and solar absorber layers to protect them. The assembly of the middle stage (Fig. S4 (b)) shows an aluminum plate (Shengjili, 10×10×0.05 cm^3), fitted into the frame from the back, which served as the condenser and attached with a paper towel evaporator. To ensure thermal contact between the last condenser and the water reservoir, a longer aluminum plate (10×15×0.05 cm^3) was used for the last stage (Fig. S4(c)). The entire TMSS prototype was assembled by fastening all eleven stages using seven sets of screws, studs and nuts (Fig. S4 (d)). The edge of each frame was lined with Teflon tape to improve the sealing. Fig. S4 (e) shows the final TMSS prototype assembly. The gap between two adjacent condensers is 5 mm (Fig. S4(e): left red box). The L-shape design at the bottom of the frame forms a self-sealing structure with the capillary wick, which allows capillary flow while preventing vapor leakage (Fig. S4(e): right red box).

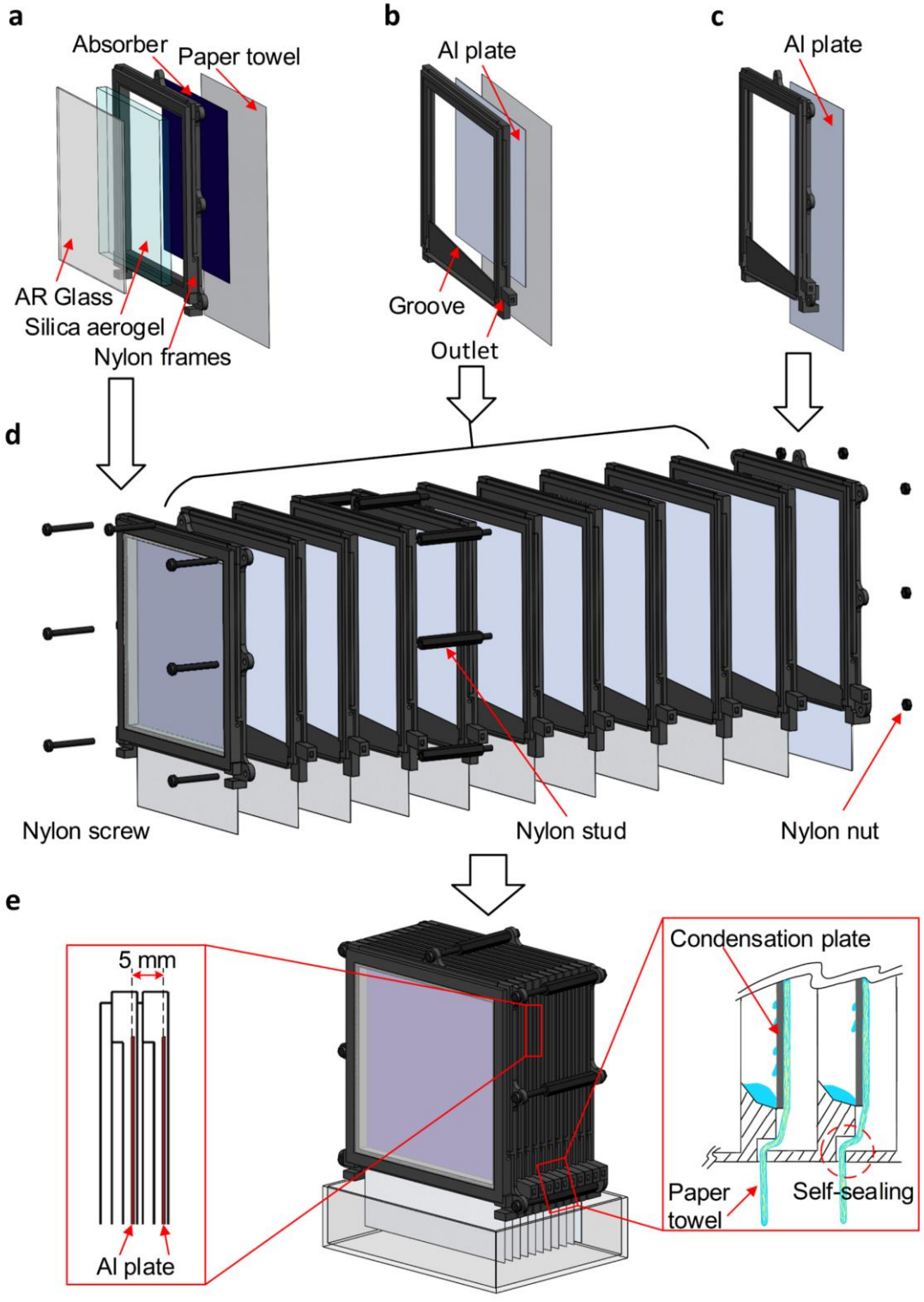

Fig. S4 Ten-stage TMSS prototype assembly. (a) Schematic of the first stage comprising a nylon frame, solar absorber, paper towel, silica aerogel and AR glass. (b) Schematic of the middle stage comprising a frame, aluminum plate and paper towel. (c) Schematic of the last stage comprising a frame and aluminum plate. (d) Exploded view of the 10-stage TMSS device showing the assembled individual stages and fasten screw-stud-nuts. (e) Assembled 10-stage TMSS prototype with a water reservoir at the bottom. Left red box: the air gap

in each stage is 5 mm. Right red box: the self-sealing design reduces vapor leakage while ensuring capillary flow.

Supplementary Note S.3

TMSS Component Preparation and Characterization

The condenser layers comprised of hydrophobic aluminum plates. The aluminum plates were first cleaned using an ultrasonic cleaner (HB-S-49MHT, KENDAL) in acetone, followed by argon plasma treatment. To enable dropwise condensation, each plate was spin-coated with ≈1 μm thick Teflon AF, and shown to have an advancing contact angle about 108.2^{o} and a receding contact angle about 103.2^{o}. The contact angle was characterized using a custom setup comprising a syringe pump (Micro4, World Precision Instruments), and a DSLR camera (EOS Rebel T3, Cannon) with a macro lens to image the droplet morphology in the advancing and receding states. The contact angle was extracted from the images using the software ImageJ.

The solar-transparent silica aerogel was synthesized by sol−gel polymerization of tetramethyl orthosilicate (TMOS, 131903, Sigma-Aldrich), using an ammonia solution (NH_3, 2.0 M in Methanol, 341428, Sigma-Aldrich) as a catalyst to promote both hydrolysis and condensation reactions. TMOS was diluted by methanol (MeOH, 322415, Sigma-Aldrich) followed by addition of NH_3 and water with a molar ratio of NH_3:TMOS:water:methanol = 0.0348:1:4:6.42. Then, the solution was gelled in a disposable polystyrene container. After two weeks of aging, the gel was taken out of the container to start solvent exchange with ethanol (EtOH, 89234−848, VWR). To dry the wet gels in EtOH without cracks, we used critical point drying with CO_2 (CPD, model 931, Tousimis). After drying, the aerogels samples were annealed at 400 °C for 24 h to maximize their transmittance. We used a piece of 9.5 cm×9.5 cm×5 mm large silica aerogel in this study. Fig. S5 shows a representative silica aerogel sample with high visible transmittance (>97%).

The direct-hemispherical transmittance of the AR glass, silica aerogel and solar absorber was measured using a UV-vis-NIR spectrophotometer (Cary 5000, Agilent) with an integrating sphere (Internal DRA-2500, Agilent) and a Fourier transform infrared (FTIR) spectrometer (5700, Nicolet) with a Pike Technologies mid-IR integrating sphere.

To determine the salinity of the purified water, the conductivity was measured using a conductivity meter with 1% accuracy of the reading (Ultrameter III, Myron L Company). The conductivity probe was first rinsed thoroughly with deionized water to eliminate any contaminants. The probe was then rinsed multiple times with the TMSS purified water. Three conductivity measurements were recorded afterwards using the probe, and the averaged result was reported.

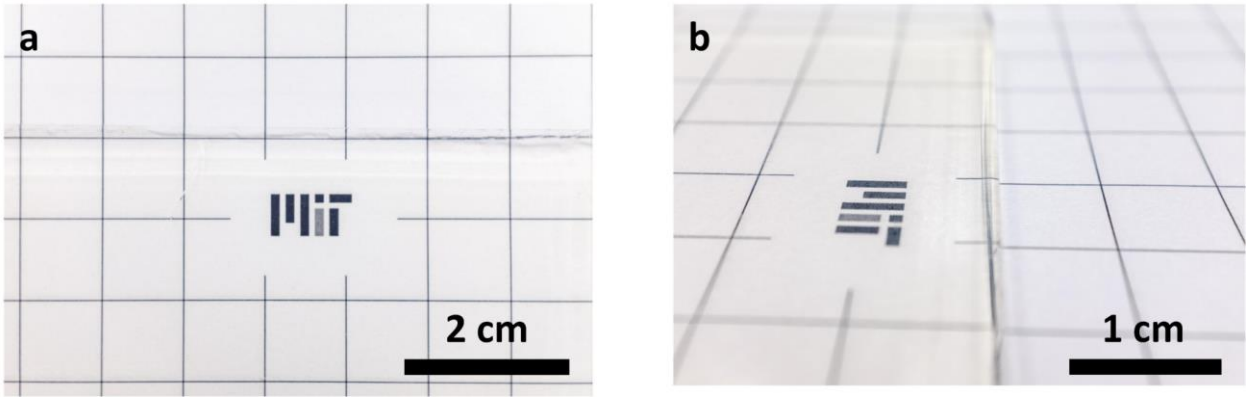

Fig. S5 Representative silica aerogel sample exhibiting high optical transmittance observed from (a) the top view (the silica aerogel sample was placed at the lower side of the field of view) and (b) the side view (the silica aerogel sample was placed at the left side of the field of view). The aerogel sample was placed over a sheet of paper with a grid pattern and MIT logo to show its transparency.

Supplementary Note S.4

Experimental Procedure

This section describes detailed procedures for the laboratory and outdoor tests. For the indoor laboratory tests, the ten-stage TMSS device was placed on a 6 cm tall acrylic box with a 6×11 cm^2 area window which allowed the capillary wicks to access and contact the water reservoir (Fig. S6). The water reservoir was placed on a balance with 0.1 g resolution (SJX6201N/E, Ohaus) which characterized the real-time mass loss during the experiment. To reduce the heat loss from the sidewalls, the TMSS prototype was surrounded with 1.27 cm thick thermal insulation having a thermal conductivity of 0.022 W m^{-1} K^{-1} (Super Tuff-R^{TM}, Dupont). A 5 cm wide funnel (made with aluminum foil) collected condensed water from the outlet of all stages and delivered to a container on the side of the acrylic box. A uniform solar flux (1000 W m^{-2}) was provided by a solar simulator (92192, Newport Oriel Inc.,). The solar flux was measured using a thermopile (818P-040-55, Newport) and recorded using a power meter (1918-C, Newport). Data acquisition equipment (34972A, Agilent), operated using LabView, recorded the temperature data from twelve K-type thermocouples and the mass loss data from the balance at five second intervals. The steady-state water production rate was evaluated from the measured mass loss curve using linear fitting after the TMSS device reached steady condition. After the 1-sun experiment, we turned off the solar simulator and continued measuring the mass loss for more than 12 hours to calibrate the dark evaporation rate.

The outdoor test (Fig. 6) was performed on the rooftop of Building 1 at MIT (Cambridge, MA, USA) on July 13, 2019 – a partly sunny day with scattered clouds. A thermal pyranometer (LP-02, Hukseflux) with the same tilt angle (30^o) as the TMSS device measured the real-time variation of solar flux over the course of the experiment. The average solar flux during the water collection process was ≈ 670 W m^{-2} while the peak solar flux at solar noon (12:40 pm local time) was ≈ 800-850 W m^{-2}. The solar absorber was initially covered using aluminum foil to avoid solar heating. The aluminum foil was removed at 11:10 am, and water flow from the first stage was first observed about 20 minutes later. During the 4.5-hour collection, ≈ 61 ml water flowed out from the device (Video S3). After the test, we collected additional water in the grooves of the stages by tilting the device. In total, 72 ml water was collected in this outdoor test.

Fig. S6 Experimental setup for laboratory tests. Simulated solar radiation from a solar simulator incident on the ten-stage TMSS device, shown here with sidewall thermal insulation to reduce heat loss and improve the overall efficiency. Twelve thermocouples measured the temperature of each stage and the ambient environment. A balance placed below the reservoir and the device, characterized the mass loss of the reservoir.

Supplementary Note S.5

Cost Analysis

The TMSS device was designed with commercially-available and low-cost materials. Here we estimate the total material cost of the device including the AR glass cover, silica aerogel, solar absorber, paper towel, aluminum plate and nylon frame. The retail cost of each part is summarized below:

- The unit price of AR glass is \$0.43/kg. We used about 0.025 kg in this device, which costs \$0.01.
- The unit price of silica aerogel is \$4/L. For a 9.5×9.5×0.5 cm^3 large silica aerogel, the corresponding cost is \$0.2. The cost estimation is based on an analysis performed by a technical consulting company (Navigant Consulting) specifically for our synthesis recipe at a production scale of 100,000 L/year. Other sources predict similar cost for monolithic silica aerogel [2].
- The unit price of the solar absorber (B-SX/T-L/Z-Z-1.88, Linuo-Paradigma, selective coating on aluminum plate) is \$6.54/m^2. We used a 0.01 m^2 large solar absorber in this work, which costs about \$0.07.
- The unit price of paper towel (Create-a-Size Paper Towels, Kirkland^{TM}) is \$0.21/m^2. In this ten-stage device, we used 10 pieces of 10×15 cm^2 large paper towel, which costs about \$0.03 in total.
- The unit price of aluminum is \$2.03/kg. The total weight of ten aluminum plates is about 0.14 kg, which costs \$0.28.
- We used nylon PA 12 which is stable at high temperatures (heat distortion temperature around 175 ^oC). The unit price of nylon PA 12 is \$4.5/kg and we used 0.211 kg for this prototype. The total cost for nylon is \$0.95.

Based on the above cost analysis for each component, the total material cost for our ten-stage TMSS device is ≈\$1.54. Detailed information about the cost of materials is summarized in Table S2.

Table S2. Summary for material cost

Item	Unit cost	Cost	Retailer
AR glass	\$0.43/kg	\$0.01	Alibaba.com
Silica aerogel	\$4/L	\$0.2	Navigant Consulting
Solar absorber	\$6.54/m^2	\$0.07	Linuo-Paradigma
Paper towel	\$0.21/m^2	\$0.03	Kirkland™
Aluminum	\$2.03/kg	\$0.28	Worldal.com
Nylon PA 12	\$4.5/kg	\$0.95	Alibaba.com
Total	--	\$1.54	--

Supplementary Note S.6

Time-dependent Mass Transport and Uncertainty Analysis

To understand the transient behavior of mass loss shown in Fig. 3(c) of the main text, we developed a time-dependent mass transport model using the experimentally measured device temperatures. The mass flux at stage *i* can be calculated from the Fick's law of diffusion,

$$m''_{evap,i} = D_a(\bar{T})\frac{\Delta c_i}{b} = D_a(\bar{T})\frac{c(T_i) - c(T_{i+1})}{b} \tag{S9}$$

where $c(T_i)$ and $c(T_{i+1})$ are the saturated vapor concentrations at the evaporator (with temperature T_i) and condenser (with temperature T_{i+1}) of the i^{th} stage, respectively. The time-dependent temperature of each stage is shown in Fig. 3(b). In this model, we considered the temperature-dependent mass diffusivity $D_a(\bar{T})$ of binary species, as per Chapman–Enskog theory,

$$D_a(\bar{T}) = \frac{A \cdot \sqrt{1/M_1 + 1/M_2}}{p\sigma_{12}^2\Omega}\bar{T}^{\frac{3}{2}} = C \cdot \bar{T}^{\frac{3}{2}} \tag{S10}$$

where *A* is an empirical coefficient, *p* is the ambient pressure, Ω is the collision integral. M_1 and M_2 are the molar mass of the two species: water and air. σ_{12} is the average collision diameter. $\bar{T} = (T_i + T_{i+1})/2$ is the average temperature of each stage. Since *C* is determined by species properties alone, we treat it as a constant for our experiments and evaluate it by fitting the one-stage experimental results – assuming a $\bar{T}^{\frac{3}{2}}$ dependence of the mass diffusivity – and then predicted the behavior of the ten-stage device.

The uncertainty in vapor flux at each stage in steady state can also be calculated using Eq. (S9), through propagation of uncertainty. The uncertainty of vapor flux arises from the temperature fluctuations,

$$\delta m'' = \sqrt{\left(D_a\frac{\delta c}{b}\right)^2 + \left(\delta D_a\,\frac{\Delta c}{b}\right)^2} \tag{S11}$$

where the uncertainty of the vapor concentration and diffusivity can be estimated as,

$$\delta c = \left.\frac{dc(T)}{dT}\right|_{\bar{T}} \delta T, \tag{S12}$$

and,

$$\delta D = \frac{3}{2} C T^{\frac{1}{2}} \delta T \tag{S13}$$

where δT is uncertainty of the temperature measured using thermocouples (1.5 ^{o}C). According to Eqs. (S11), (S12) and (S13), the uncertainty of the measured vapor flux increases as temperature increases – as shown in Fig. 3(d).

Supplementary Note S.7

Supplementary Video Description

- **Video S1** shows the start-up process of the ten-stage TMSS device in the laboratory test. Water began to flow out of the first stage 8 minutes after solar exposure. The following stages were activated gradually and the entire device reached the steady operation after 100 minutes, with water flowing out of all ten stages simultaneously.

- **Video S2** shows the steady-state operation of the ten-stage TMSS device in the laboratory test. Water flowed out of all ten stages simultaneously and collected in a separate container.

- **Video S3** shows the water collection of the ten-stage TMSS device in the outdoor test. The experiment was performed on the rooftop of MIT Building 1 (Cambridge, MA, USA) on July 13, 2019. The video started at 11:10 am (local time) and ended around 4:00 pm (local time). The top left zoom-in window shows the water flowing out of each stage during the operation. The bottom left zoom-in window shows the corresponding rise of water level in the graduated cylinder. The right window shows the overall water collection process where water began to flow out 20 minutes after the experiment started. Real-time fluctuations in the incident solar flux due to the scattered clouds can be observed through the moving shadows. Approximately 61 ml water flowed directly into the graduated cylinder during the test. After the experiment, we tilted the TMSS device to collect the remaining water in the device – adding up to ≈72 ml water in total.

REFERENCES

[1] L. Zhang, Z. Xu, B. Bhatia, B. Li, L. Zhao, E. N. Wang, Modeling and performance analysis of high-efficiency thermally-localized multistage solar stills, Submitted.

[2] A. F. Mills, *Heat Transfer*, 2nd ed. (Prentice Hall, 1999).

[3] M.A. Aegerter, N. Leventis, M.M. Koebel, Aerogels handbook, Springer, 2011. doi:10.1007/978-1-4614-1957-0.